Mathematical Biosciences and Engineering

http://www.aimspress.com/journal/mbe

MBE, 23(7): 2055–2082.
DOI: 10.3934/mbe.2026075
Received: 30 January 2026
Revised: 27 May 2026
Accepted: 15 June 2026
Published: 10 July 2026

Research article

Modeling the relation between intraocular pressure and human trabecular meshwork fluid-mechanical properties

Riccardo Sacco[1,*], Greta Chiaravalli[2], Giovanna Guidoboni[3], Anita Layton[4], Gal Antman[5], Alice Verticchio[6], Brent Siesky[6], Thomas A. Ciulla[7] and Alon Harris[6]

[1] Dipartimento di Matematica, Politecnico di Milano, Milano 20133, Italy
[2] Dipartimento di Fisica, Politecnico di Milano, Milano 20133, Italy
[3] Maine College of Engineering and Computing, University of Maine, Orono 04469, USA
[4] Department of Applied Mathematics, University of Waterloo, Waterloo N2L 3G1, Canada
[5] Faculty of Medicine, Tel Aviv University, Tel Aviv 6997801, Israel
[6] Department of Ophthalmology, Icahn School of Medicine at Mount Sinai Hospital, New York 10029, USA
[7] School of Medicine, Indiana University, Indianapolis 46202, USA

* **Correspondence:** Email: riccardo.sacco@polimi.it.

Abstract: Elevated introcular pressure (IOP) is a major risk factor for primary open angle glaucoma (POAG), the second leading cause of blindness worldwide. In this article, we investigate the relation between IOP increase and fluid-mechanical properties of the trabecular meshwork (TM), which is the main pathway of aqueous humor (AH) outflow in the human eye. TM is represented as an axisymmetric deformable biphasic porous medium (solid and fluid) with hydraulic permeability nonlinearly depending on the local AH pressure. Solving Darcy's law provides a TM hydraulic resistance (TMR) depending on the radial pressure drop, while TM stiffness is included multiplying the TMR by a shape function of TM Young's modulus constructed using postmortem measurements of human eye outflow facility. Simulations of AH flow based on an electric equivalent scheme of the eye indicate that TMR increases with TM stiffness, leading to a progressive increase of IOP until over the upper limit of the normal IOP range. The obtained results shed light on the impact of microscopic properties of the eye on its macroscopic function, and support the integration of experimental studies, mathematical modeling, and data analysis to develop an optimized patient-specific therapy to cure POAG.

Keywords: mathematical modeling; simulation; glaucoma; aqueous humor; biphasic porous media; stiffness; hydraulic resistance

1. Introduction

Primary open angle glaucoma (POAG, also referred to in the text as glaucoma) is a multifactorial disease representing the second leading cause of legal blindness worldwide [1]. Despite the triggering mechanisms of glaucoma are far from being completely unraveled, a generally established consensus identifies an elevated intraocular pressure (IOP) as one of the major risk factors for glaucoma onset and progression [2], with a widely accepted range of normal IOP between 10 and 21 mmHg [3].

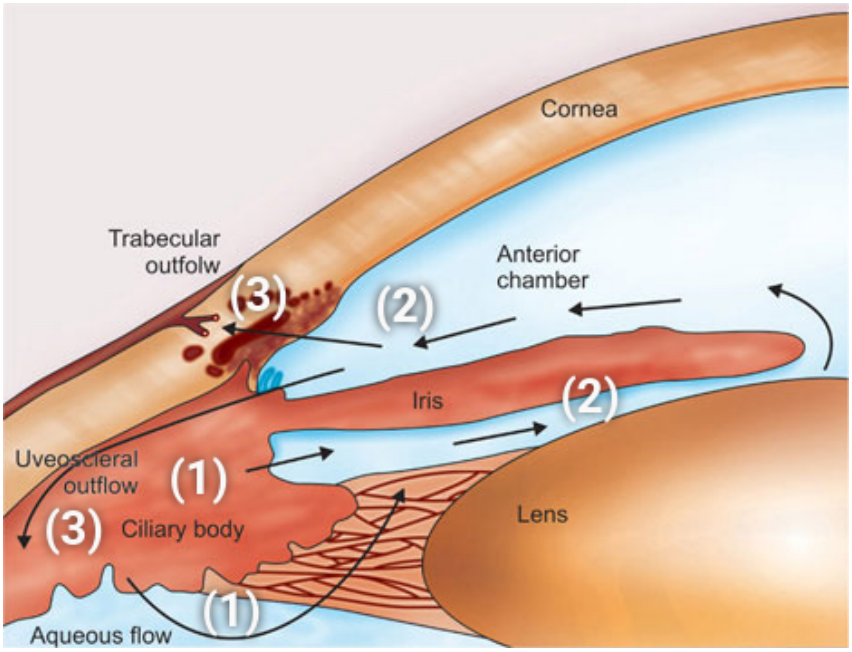

Figure 1. Schematic representation of the process of IOP formation. Reprinted from R. Ramakrishnan et al., Diagnosis & Management of Glaucoma, Chapter 9 Aqueous Humor Dynamics, 10.5005/jp/books/11801_9, (2013) [4]; used in accordance with the Creative Commons Attribution (CC BY) license.

IOP is the result of the steady-state balance among the phases of production, flow, and outflow of aqueous humor (AH, see [5–7]), a transparent watery fluid that occupies the anterior segment of the eye and has the main function of keeping the eyeball inflated at the appropriate pressure [8]. The three phases are illustrated in Figure 1 and constitute the process of **AH dynamics**:

(Ph.1) : AH is secreted by the ciliary processes of the ciliary body (CB) into the posterior chamber (PC).

(Ph.2) : AH flows from the PC into the anterior chamber (AC) crossing through the pupil.

(Ph.3) : AH is drained out into the eye peripheral vasculature through two principal outflow routes, the trabecular meshwork (TM) and uveoscleral (UV) outflow pathways.

To translate the physiological mechanisms of IOP formation into a mathematical model, we leverage the analogy between fluid and electric variables illustrated in [9, Section 10.5.1] and introduce the

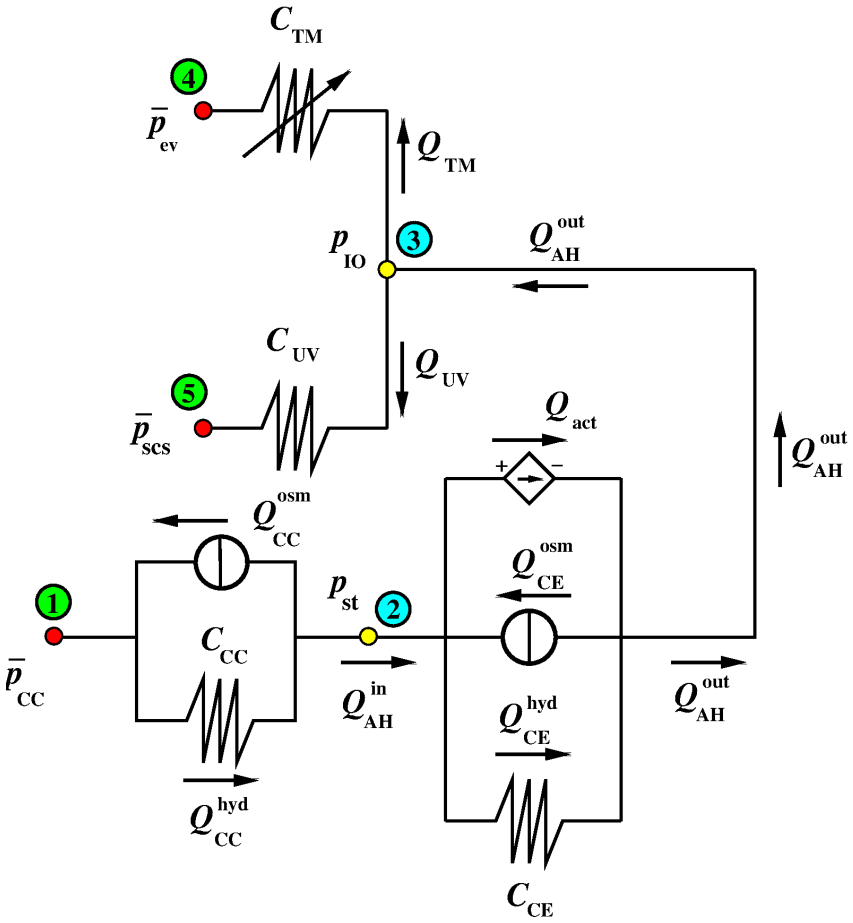

Figure 2. Electric equivalent scheme of the anterior segment of the eye. The meaning of the symbols is described in Section 2.

electric equivalent scheme of the anterior segment of the eye shown in Figure 2. The circuit consists of five nodes, indicated with numbered circles, divided in two groups on the basis of their color. At the cyan-colored nodes (② and ③), the AH fluid pressure is unknown, whereas the electrochemical variables (neutral and charged solute concentrations, electric potential) are given data. At the red-colored nodes (①, ④ and ⑤), the AH fluid pressure and electrochemical variables are given data. Referring to Section 2 for a detailed explanation of symbols and variables, the application of Kirchhoff current law at the cyan-colored nodes ② and ③ gives rise to the following nonlinear system of algebraic equations:

$$\mathbf{F}(\mathbf{X}) = \mathbf{0}, \tag{1.1a}$$

where $\mathbf{X} = [p_{\mathrm{st}},\ p_{\mathrm{IO}}]^T$ is the column vector of the unknown pressures in the ciliary stroma, p_{st}, and in the aqueous side, p_{IO} (the IOP), while $\mathbf{F}(\mathbf{X}) = [F_1(\mathbf{X}),\ F_2(\mathbf{X})]^T$, $\mathbf{0} = [0,\ 0]^T$ and:

$$F_1(\mathbf{X}) = -Q_{\mathrm{AH}}^{\mathrm{in}}(\mathbf{X}) + Q_{\mathrm{AH}}^{\mathrm{out}}(\mathbf{X}), \tag{1.1b}$$

$$F_2(\mathbf{X}) = -Q_{\mathrm{AH}}^{\mathrm{out}}(\mathbf{X}) + Q_{\mathrm{TM}}(\mathbf{X}) + Q_{\mathrm{UV}}(\mathbf{X}), \tag{1.1c}$$

with the "-" and "+" signs denoting a current entering or leaving the node, respectively.

To solve (1.1), in Section 3, we provide the expression of the AH volumetric flow rates (VFR) $Q_{\mathrm{AH}}^{\mathrm{in}}$, $Q_{\mathrm{AH}}^{\mathrm{out}}$, Q_{TM}, and Q_{UV} (units: $\mu\mathrm{Lmin}^{-1}$) as a function of p_{st}, p_{IO} and any measurable parameters describing processes (**Ph.1**)–(**Ph.3**), in such a way that the model represented by (1.1) can be used as a supporting tool to help inform whether the most appropriate therapeutic approach may be either (a) to reduce AH production and/or (b) to increase AH outflow. To shed light on the efficacy of these approaches, we focus in this article on the connection between the TM hydraulic resistance $R_{\mathrm{TM}} = (C_{\mathrm{TM}})^{-1}$ and p_{IO} (see [10–12]). Even though TM is recognized to be a pressure-dependent pathway for AH outflow [13–15], neither the exact mechanisms by which TM outflow structures sense and respond to biomechanical forces are fully understood, nor the interplay between R_{TM} and changes in the IOP have been theoretically investigated. To help fill these gaps, in Sections 4 and 5, we introduce a geometrical model of the TM tissue and a mathematical model of the TM outflow pathway based on the following assumptions:

A.1 The TM tissue is an axisymmetric deformable porous medium, mathematically represented by a heterogeneous mixture with solid and fluid constituents (or phases, see [9, Sections 8.2 and 12.2] and [16]).

A.2 The TM hydraulic permeability is an exponential function of TM dilatation [17, 18].

In Section 6, we use **A.1** and **A.2** to solve Darcy's equation under Dirichlet boundary conditions for p_{IO} at the endpoints of the TM radial thickness, obtaining a compact expression of R_{TM} that nonlinearly depends on the pressure drop $\Delta p = p_{\mathrm{IO}} - \overline{p}_{\mathrm{ev}}$. The dependence of R_{TM} on the TM stiffness is accounted for through the multiplication of the compact expression of R_{TM} by a dimensionless shape function of the TM Young's modulus E_{TM} constructed using the postmortem measurements of human eye outflow facility conducted and analyzed in [19]. Inserting the proposed model of R_{TM} into (1.1) allows us to perform a parametric analysis of IOP and AH flow as a function of E_{TM}. The computational algorithm that is used to numerically solve the nonlinear system (1.1) is illustrated in Section 7, where we first write the nonlinear system in matrix form and then we introduce a Richardson-type fixed-point (FP) iteration for its solution up to a user-defined tolerance. Section 8 describes the results of simulations conducted using the model parameters illustrated in Appendices A and B and the FP iteration illustrated in Section 7. Model predictions indicate that R_{TM} increases with TM stiffness, leading to a progressive increase of IOP until over the upper limit 21 mmHg of the normal IOP range. These findings are discussed in Section 9 and confirm the experimental and theoretical studies which suggest that human trabecular meshwork stiffness in normal eyes may be different (typically larger) from that in glaucomatous eyes and that this difference may confer to TM stiffness a significant role in the pathogenesis of ocular hypertension in glaucoma (see [19–21]). Summarizing conclusions on the research achievements as well as model limitations and perspectives are addressed in Section 10.

2. The electric equivalent representation of AH dynamics

Table 1. Table of equivalence between electric and fluid variables.

Electric variable	Units	Fluid variable	Units	Symbol
Current	$\mathrm{Coul\,s}^{-1}$	Volumetric flow rate	$\mu\mathrm{L\,min}^{-1}$	Q
Voltage	V	Pressure	mmHg	p

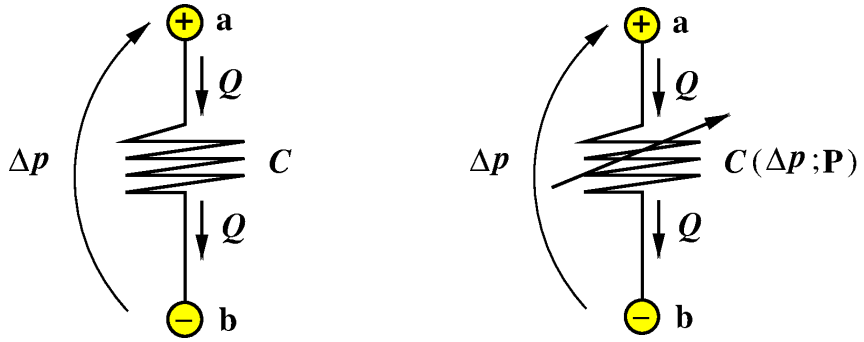

Figure 3. Left panel: linear time-invariant resistor. Right panel: nonlinear time-invariant resistor. In both cases, C is the hydraulic conductance (units: μL (mmHg min)$^{-1}$); Q is the volumetric flow rate (units: μL min^{-1}); $\Delta p = p_a - p_b$ is the pressure difference across the conductance (unit: mmHg). In both circuit elements, C, Q, and Δp are related by the fluid analog of Ohm's law. In the nonlinear resistor (right panel), C is not a constant quantity (as in the left panel) but nonlinearly depends on Δp and a vector of biophysical parameters $\mathbf{P}$.

The electric circuit illustrated in Figure 2 leverages the analogy between electric and fluid variables described in [9, Section 10.5.1] and summarized in Table 1. According to this analogy, the relation between the pressure difference Δp across the linear time-invariant resistor shown in Figure 3 (left panel) and the volumetric flow rate Q of the fluid flowing from node ⓐ to node ⓑ is the fluid equivalent of Ohm's law

$$Q = C\,\Delta p, \tag{2.1a}$$

where C is a linear hydraulic conductance, also referred to as hydraulic facility (units: μL (mmHg min)$^{-1}$). Expression (2.1a) can be used to mathematically represent $Q_{\mathrm{CC}}^{\mathrm{hyd}}$, $Q_{\mathrm{CE}}^{\mathrm{hyd}}$, and Q_{UV}. A transversal arrow is used to represent a nonlinear conductance (right panel of Figure 3) in which C depends nonlinearly on Δp (and on other physical parameters). In this case, the fluid equivalent of Ohm's law becomes the following:

$$Q = C(\Delta p; \mathbf{P})\,\Delta p, \tag{2.1b}$$

where $\mathbf{P}$ is a vector of biophysical parameters. Expression (2.1b) can be used to mathematically represent Q_{TM}. If $C \neq 0$, then it is possible to express Ohm's law in the following equivalent form:

$$\Delta p = R\,Q, \tag{2.1c}$$

where

$$R = (C)^{-1} \tag{2.1d}$$

is the hydraulic resistance of the resistor (unit: mmHg (μL min)$^{-1}$). The nonlinear version of Ohm's law (2.1c) is as follows:

$$\Delta p = R(\Delta p; \mathbf{P})\,Q. \tag{2.1e}$$

The various objects appearing in Figure 2 can be classified as follows:

- Boundary nodes (red color, ①, ④ and ⑤), connected to ground through an independent voltage source that fixes the value of the pressure (units: mmHg).
- Internal nodes (cyan color, ② and ③), where the pressure is unknown.
- Linear and nonlinear hydraulic resistors, with the nonlinear conductance represented by a crossing black arrow.
- Two current sources, Q_{CC}^{osm} and Q_{CE}^{osm} (units: $\mu L\,min^{-1}$), depending on the molar densities of ions, neutral solutes, neutral and charged proteins, and on the values of the electric potential in the ciliary capillaries, in the ciliary stroma, and in the aqueous side.
- A current source Q_{act} (units: $\mu L\,min^{-1}$) depending on Q_{AH}^{in} and represented with a romboidal symbol.

Node ① is connected to the ground by the voltage source $\overline{p}_{CC}$ modeling blood pressure into the fenestrated ciliary capillaries (FCCs). The process of AH ultrafiltration across the FCC wall (see [7, 22]) is represented by the parallel connection between the hydraulic conductance C_{CC} and the current source Q_{CC}^{osm}. Notably, Q_{CC}^{osm} has an opposite direction with respect to Q_{CC}^{hyd}, according to Starling's law of ultrafiltration, which expresses the balance of hydrostatic and osmotic pressures pushing AH out and in the capillary, respectively (see [23]). Node ② represents the fluid pressure in the ciliary stroma which is the intermediate region between the ciliary capillaries and the ciliary epithelium (see [8]), whereas node ③ represents the fluid pressure in the aqueous side. The circuit block connecting node ② to node ③ is a current partitioner since it divides the input current Q_{AH}^{in} into three distinct contributions: an aqueous VFR Q_{CE}^{hyd} representing water flow across the hydraulic conductance C_{CE} driven by a hydraulic pressure gradient; an aqueous VFR Q_{CE}^{osm} representing passive water flow across the CE due to an electrochemically driven osmotic pressure gradient; an aqueous VFR Q_{act} representing flow across the CE due to an osmotic pressure gradient driven by active ion secretion. The wire connecting the current partitioner block to node ③ and node ③ to the outflow block represents the mechanism of AH flow. In our lumped parameter model, we neglect any drag viscous forces opposing to fluid motion between posterior and anterior chambers; we refer to [24] for a different treatment of this aspect. The outflow block of the circuit is a current partitioner dividing the output current Q_{AH}^{out} into two contributions: an aqueous VFR Q_{TM} representing water flow across the trabecular meshwork and an aqueous VFR Q_{UV} representing water flow across the uveoscleral pathway. The nonlinear hydraulic conductance C_{TM} depends on the pressure difference $\Delta p = p_{IO} - \overline{p}_{ev}$ and on the TM stiffness represented by the TM Young's modulus E_{TM}. This assumption is consistent with the conjecture that the fluid-mechanical properties of the TM act in a different manner in normal and glaucomatous eyes (see [19–21, 25]). The linear time-invariant hydraulic conductance C_{UV} represents the pressure-independent water flow across the UV tissue into the SCS (see [13, 15]).

3. Modeling current sources in AH production

In this section, we illustrate the mathematical expressions of the current sources Q_{CC}^{osm}, Q_{CE}^{osm}, and Q_{act} introduced in Figure 2. Let U denote a real-valued variable and define the transepithelial difference $\Delta U := U^{st} - U^{aq}$, where U^{st} and U^{aq} are the values of U in the ciliary stroma and aqueous side,

respectively. Let us introduce the electrochemical potential of ion α (see [9, Section 13.6.3]) as follows:

$$\varphi_\alpha^{\mathrm{ec}} = \psi + \frac{V_{th}}{z_\alpha} \ln\left(\frac{c_\alpha}{c_{\mathrm{ref}}}\right), \tag{3.1a}$$

where ψ is the electric potential (units: V), c_α is the molar density of ion α (units: mM), $V_{th} = \frac{RT}{F}$ is the thermal voltage (units: V), with R, T, and F denoting the gas constant, the absolute temperature, and Faraday's constant, respectively, z_α is the chemical valence of ion α and c_{ref} is a reference value for ion molar densities (units: mM). Setting $U = \varphi_\alpha^{\mathrm{ec}}$, the transepithelial electrochemical potential difference is as follows:

$$\Delta\varphi_\alpha^{\mathrm{ec}} = \Delta\psi + \frac{V_{th}}{z_\alpha} \ln\left(\frac{c_\alpha^{\mathrm{st}}}{c_\alpha^{\mathrm{aq}}}\right), \tag{3.1b}$$

where the superscripts "st" and "aq" denote the ciliary stroma and the aqueous side, respectively. Then, we define the molar flux density (units: $\mathrm{mol\,m^{-2}\,s^{-1}}$) representing passive ion motion (see [9, Section 13.6.3]) as follows:

$$\mathbf{f}_\alpha^{\mathrm{pass}} = \frac{\mathbf{J}_\alpha^{\mathrm{pass}}}{F z_\alpha} = -\mu_\alpha^{el} \frac{|z_\alpha|}{z_\alpha} c_\alpha \nabla\varphi_\alpha^{\mathrm{ec}}, \tag{3.2a}$$

where μ_α^{el} is the electric mobility of ion α (units: $\mathrm{m^2\,V^{-1}\,s^{-1}}$), proportional to the ionic diffusivity D_α (units: $\mathrm{m^2\,s^{-1}}$) through Einstein's relation

$$D_\alpha = \mu_\alpha^{el} \frac{V_{th}}{|z_\alpha|}. \tag{3.2b}$$

We introduce the first-order approximation of the projection of the vector field $\mathbf{f}_\alpha^{\mathrm{pass}}$ along the outward normal unit vector to the CE as follows:

$$f_{\alpha,\mathrm{CE}}^{\mathrm{pass}} = \mu_\alpha^{el} \frac{|z_\alpha|}{z_\alpha} \langle c_\alpha \rangle_{\mathrm{CE}} \frac{\Delta\varphi_\alpha^{\mathrm{ec}}}{t_{\mathrm{CE}}}, \tag{3.3}$$

where t_{CE} is the thickness of the CE and

$$\langle c_\alpha \rangle_{\mathrm{CE}} := \frac{\overline{c}_\alpha^{\mathrm{pl}} + \overline{c}_\alpha^{\mathrm{aq}}}{2}. \tag{3.4}$$

Using (3.2b) and (3.1b) into (3.3), we obtain the following:

$$f_{\alpha,\mathrm{CE}}^{\mathrm{pass}} = z_\alpha \frac{D_\alpha}{t_{\mathrm{TM}}} \frac{\langle c_\alpha \rangle_{\mathrm{CE}}}{V_{th}} \left[\Delta\psi + \frac{V_{th}}{z_\alpha} \ln\left(\frac{c_\alpha^{\mathrm{st}}}{c_\alpha^{\mathrm{aq}}}\right)\right]. \tag{3.5a}$$

Introducing the diffusional permeability $P_\alpha = D_\alpha / t_{\mathrm{CE}}$ of the CE to ion α (units: $\mathrm{m\,s^{-1}}$) and using the fact that $V_{th} = (RT)/F$, (3.5a) becomes

$$f_{\alpha,\mathrm{CE}}^{\mathrm{pass}} = \omega_\alpha \Delta\Pi_\alpha^{\mathrm{ec}}, \tag{3.5b}$$

where

$$\omega_\alpha := \frac{D_\alpha}{t_{\mathrm{CE}}} \frac{1}{RT} = \frac{P_\alpha}{RT} \tag{3.5c}$$

represents the permeability coefficient of ion α (see [26], Eq (30), units: $\mathrm{m\,mol\,J^{-1}\,s^{-1}}$). The quantity

$$\Delta\Pi_\alpha^{\mathrm{ec}} = \Delta\Pi_\alpha^{\mathrm{el}} + \Delta\Pi_\alpha^{\mathrm{ch}} \tag{3.5d}$$

is the transepithelial electrochemically driven pressure difference of ion α (units: mmHg), where

$$\Delta\Pi_\alpha^{\mathrm{el}} := F z_\alpha \langle c_\alpha \rangle_{\mathrm{CE}} \Delta\psi, \tag{3.5e}$$

$$\Delta\Pi_\alpha^{\mathrm{ch}} := R\,T \langle c_\alpha \rangle_{\mathrm{CE}} \ln\left(\frac{c_\alpha^{\mathrm{pl}}}{c_\alpha^{\mathrm{aq}}}\right) \tag{3.5f}$$

are the transepithelial electrically and chemically driven pressure differences of ion α, respectively.

Remark 1. *Relations* (3.5) *are the generalization of Eq (32) in [26].*

It is useful to recall van't Hoff relation which expresses the pressure π_c (units: mmHg) exerted by a solute having molar density equal to c (units: mM)

$$\pi_c = K_c R T c, \tag{3.6}$$

where $K_c = 7.50062 \cdot 10^{-3}$ is the conversion factor from $\mathrm{N\,m^{-2}}$ to mmHg. Using (3.6), the total electrochemically driven osmotic pressure difference across the CE is as follows:

$$\Delta\Pi_{tot}^{\mathrm{ec}} = \sum_\alpha \sigma_\alpha \Delta\Pi_\alpha^{\mathrm{ec}} + \sum_\beta \sigma_\beta \Delta\Pi_\beta + \sum_\gamma \sigma_\gamma \Delta\Pi_\gamma + \sum_X \sigma_X \Delta\Pi_X, \tag{3.7a}$$

where

$$\Delta\Pi_\beta = RT\Delta c_\beta, \tag{3.7b}$$

$$\Delta\Pi_\gamma = RT\Delta c_\gamma, \tag{3.7c}$$

$$\Delta\Pi_X = RT\Delta c_X, \tag{3.7d}$$

denote the transepithelial pressure differences due to a low molecular weight neutral solute β, a high molecular weight neutral solute γ, and an electro-neutralizing protein X. The quantities σ_α, σ_β, σ_γ, and σ_X are the reflection coefficient across the CE of ion α, of the solutes β and γ and of the neutralizing protein X, respectively. The application of Ohm's law (2.1a) yields the following expression of the current source associated with the electrochemically driven transepithelial pressure difference

$$Q_{\mathrm{memb}}^{\mathrm{osm}} = C_{\mathrm{memb}}^{\mathrm{hyd}} \Delta\Pi_{tot}^{\mathrm{ec}}, \tag{3.8}$$

where the subscript "memb" takes the values CC and CE, respectively. According to [27], active secretion is thought to be the major contributor to aqueous formation, being responsible for approximately 80% to 90% of the total aqueous humor formation. This biophysical conjecture can be mathematically modeled by the following relation:

$$Q_{\mathrm{act}} = \mathcal{K}_{\mathrm{act}} Q_{\mathrm{AH}}^{\mathrm{in}}, \tag{3.9}$$

where $\mathcal{K}_{\mathrm{act}}$ is a parameter expressing the fraction of AH water flux produced by the active secretion mechanisms (with $0 < \mathcal{K}_{\mathrm{act}} < 1$).

4. Modeling the microstructure of the trabecular meshwork

In this section, we describe the microstructure of the TM and the assumptions on the geometrical and functional representation of the TM used to simulate AH dynamics.

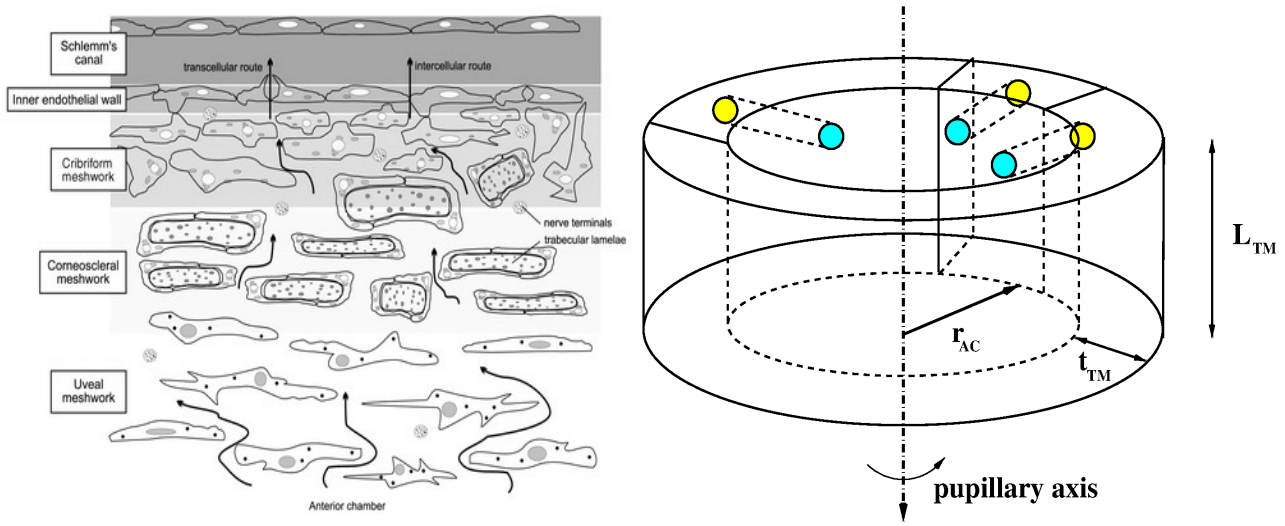

Figure 4. Left panel: schematic view of the 2D cross-section of the TM. The pupillary axis is aligned with the horizontal direction in the figure. Reprinted from A. Llobet, X. Gasull and A. Gual, Understanding Trabecular Meshwork Physiology: A Key to the Control of Intraocular Pressure? 10.1152/nips.01443.2003 (2003) [28]; used in accordance with the Creative Commons Attribution (CC BY) license. Right panel: radially symmetric 3D geometry of the TM. The cyan circles represent the pore mouth in contact with the AC whereas the yellow circles represent the pore mouth in contact with the inner endothelial wall of the TM.

The left panel of Figure 4 illustrates the microstructure of the TM tissue and indicates that the TM is a porous medium composed by the superposition of three layers; in order, proceeding radially from the AC towards the inner endothelial wall and the Schlemm canal: (a) the uveal meshwork; (b) the corneoscleral meshwork; and (c) the cribriform (or juxtacanalicular, JCT) meshwork (see [28, 29]). Each layer is characterized by the presence of extracellular material and interstitial pores across which the AH mixture percolates to exit out into the episcleral vein. The intercellular space available for AH flow within each layer varies significantly proceeding from (a) to (c), resulting in a hydraulic resistance in the uveal and corneoscleral meshwork that can be considered to be negligible compared to that of the juxtacanalicular meshwork (see [30]). The right panel of Figure 4 illustrates the geometrical and structural representation of the TM. We remark that this representation is highly simplified and key anatomical features which are known to influence the AH outflow resistance, such as the spatially varying porosity of the JCT and the accumulation of extracellular matrix waste products (see [31]), are not explicitly accounted for. These aspects of TM physiology will be considered in a subsequent, more advanced, version of the model proposed in the present article. The above considerations can be summarized in the following list of assumptions which add up to Assumptions **A.1** and **A.2** introduced in Section 1:

A.3 The hydraulic resistance due to the uveal and corneoscleral meshwork is neglected, in such a way

that resistance to AH flow is due only to the juxtacanalicular meshwork.

A.4 The TM geometry, illustrated in the right panel of Figure 4, is a 3D ring with axial length in the direction of the pupillary axis s equal to L_{TM}, while in the direction of the radial axis r the internal radius is equal to r_{AC} and the external radius equal to $r_{\mathrm{AC}} + t_{\mathrm{TM}}$, having denoted by t_{TM} the radial thickness of the TM (see [16]).

A.5 The porous microstructure of the TM tissue consists of an array of cylinders with radial length equal to t_{TM} and radius r_p.

A.6 The mechanical stiffness of the solid constituent of the TM is represented by the TM Young's modulus E_{TM} (units: kPa).

A.7 The dilatation ε of the TM solid constituent is small and is expressed by the following relation:

$$\varepsilon(p(r)) = -\frac{p(r) - p_{\mathrm{ev}}}{p_{\mathrm{IO,\,b}} - p_{\mathrm{ev}}} \qquad r \in \overline{\Omega}_r, \tag{4.1}$$

where $p = p(r)$ is the fluid pressure at the radial coordinate r, $p_{\mathrm{IO,\,b}}$ is the value of IOP in baseline conditions (units: mmHg), and $\Omega_r = (r_{\mathrm{AC}},\ r_{\mathrm{AC}} + t_{\mathrm{TM}})$.

5. Mathematical model of AH in the TM

Based on the description of the TM microstructure conducted in Section 4, the model of the interaction between AH flow and mechanical deformation of the TM consists of the following differential system in mixed form for the dependent variables p and V:

$$\frac{1}{r}\frac{d}{dr}(r\,V) = 0, \qquad r \in \Omega_r, \tag{5.1a}$$

$$\frac{\mu_{fl}}{\kappa(p(r))}V + \frac{dp}{dr} = 0, \qquad r \in \Omega_r. \tag{5.1b}$$

Equation (5.1a) is the balance of mass of the TM fluid constituent, while Eq (5.1b) is the definition of Darcy's fluid velocity $\mathbf{v}$. The quantity κ is the hydraulic permeability of the TM (units: m^2).

5.1. Modeling the hydraulic permeability of the TM

The following expression is adopted for the TM hydraulic permeability κ:

$$\kappa(p(r)) = \kappa_0 \exp\left[M\varepsilon(p(r))\right] = \kappa_0 \exp\left[-M\left(\frac{p(r) - p_{\mathrm{ev}}}{p_{\mathrm{IO,b}} - p_{\mathrm{ev}}}\right)\right], \qquad r \in \overline{\Omega}_r. \tag{5.2}$$

The quantity κ_0 represents the TM intrinsic hydraulic permeability and is described by the following equation (see [29, 32]):

$$\kappa_0 = \frac{\Phi\, d_p^2}{16\, C_K}, \tag{5.3}$$

where Φ is the porosity of the TM tissue (defined as the ratio of fluid volume to the total volume of the TM), d_p is the diameter of each pore (units: m), and C_K is the Kozeny constant, accounting for pore tortuosity effects (taken equal to 5 for the TM tissue). The quantity μ_{fl} is the dynamic viscosity of

the fluid (units: mmHg s), while M is a yet unspecified positive constant. Relation (5.2) is used in the mathematical modeling of articular cartilage (see [17, 18, 33]). For other examples of models of κ that nonlinearly depend on the dilatation of the solid constituent of a soft biological tissue, such as the retina, we refer to [34, 35].

5.2. Mechanical interpretation of the model for TM hydraulic permeability

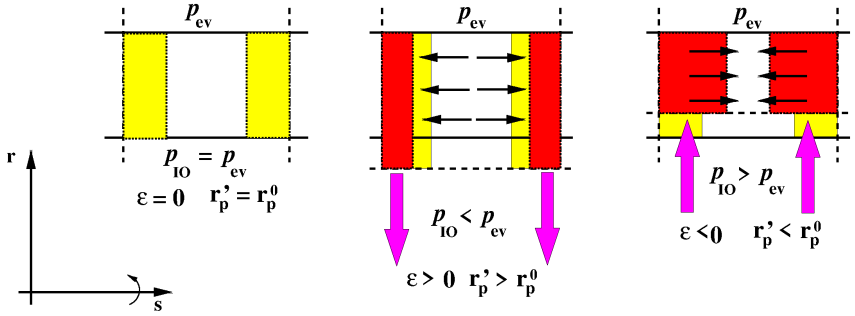

Figure 5. Schematic representation of the state of deformation of an elementary volume of the TM as a function of the values of p_{IO} and p_{ev}. The yellow and red colors represent the TM tissue in the undeformed and deformed configurations, respectively. Left panel: $p_{IO} = p_{ev}$. Middle panel: $p_{IO} < p_{ev}$. Right panel: $p_{IO} > p_{ev}$.

To give a qualitative idea of the effect of pressure difference on TM permeability, we schematically illustrate in Figure 5 the undeformed and deformed configurations of an elementary volume of TM as a function of the pressures acting on the surfaces facing the aqueous side (bottom) and episcleral side (top). The quantities r_p^0 and r_p' denote the pore radius in the undeformed and deformed configurations, respectively. The vertical dashed lines are reflecting artificial boundaries to isolate the elementary volume from the remainder of the TM tissue. The symbols r and s represent the radial and pupillary axes of the eye, respectively. We see that in the case where $p_{IO} = p_{ev}$ (left panel) there is no net pressure on the TM so that, consistent with Eq (4.1), we have $\varepsilon = 0$ and $\kappa = \kappa_0$. In the case where $p_{IO} < p_{ev}$ (middle panel), there is a net pressure (tensile stress) which pulls the TM towards the bottom producing a (small) radial elongation of the radial thickness of the tissue. Because of compressibility, the TM tissue undergoes a lateral deformation which shrinks the tissue perpendicularly to the radial direction, slightly enlarging the pore radius from the undeformed value r_p^0 to a deformed value $r_p' > r_p^0$. According to Eqs (4.1) and (5.2), this mechanical configuration corresponds to $\varepsilon > 0$ and $\kappa > \kappa_0$. Conversely, if $p_{IO} > p_{ev}$ (right panel), there is a net pressure (compression stress) which pushes the TM towards the top producing a (small) radial reduction of the radial thickness of the tissue. Because of compressibility, the TM tissue undergoes a lateral deformation which elongates the material volume perpendicularly to the radial direction, slightly diminishing the pore radius from the undeformed value r_p^0 to a deformed value $r_p' < r_p^0$. According to Eqs (4.1) and (5.2), this mechanical configuration corresponds to $\varepsilon < 0$ and $\kappa < \kappa_0$.

6. Modeling the TM hydraulic resistance R_{TM}

In this section, we solve the AH microscale model equations (5.1) to obtain a compact expression of the hydraulic resistance of the TM that can be used in the equivalent electric representation described in Section 2.

6.1. Including fluid pressure in the model for R_{TM}

Mass conservation (5.1a) yields

$$V(r) = \frac{C_v}{r}, \qquad r \in \Omega_r, \tag{6.1a}$$

where C_v is an arbitrary integration constant (units: $\mathrm{m^2 s^{-1}}$). Replacing (6.1a) into Darcy's equation (5.1b) gives rise to the following differential equation for the fluid pressure p:

$$\frac{dp(r)}{dr} = -\frac{\mathcal{A}}{r}\exp(\mathcal{B}r), \qquad r \in \Omega_r, \tag{6.1b}$$

where

$$\mathcal{A} := \frac{C_v \mu_{fl}}{\kappa_0}\exp\left(-\frac{M p_{\mathrm{ev}}}{\Delta p_b}\right), \tag{6.1c}$$

$$\mathcal{B} := \frac{M}{\Delta p_b}, \tag{6.1d}$$

having set $\Delta p_b := p_{\mathrm{IO,b}} - p_{\mathrm{ev}}$. Integrating (6.1b) yields

$$p(r) = -\frac{1}{\mathcal{B}}\ln\left[-\mathcal{B}\left(C_p - \mathcal{A}\ln(r)\right)\right], \qquad r \in \Omega_r, \tag{6.1e}$$

where C_p is an arbitrary constant. Enforcing the boundary conditions:

$$p(r_{\mathrm{AC}}) = p_{\mathrm{IO}}, \tag{6.1f}$$

$$p(r_{\mathrm{AC}} + t_{\mathrm{TM}}) = p_{\mathrm{ev}}, \tag{6.1g}$$

and using (6.1c) gives

$$C_v = \frac{\kappa_0}{\mu_{fl}} \times \left(\mathrm{Be}\left[-M\frac{\Delta p}{\Delta p_b}\right]\right)^{-1} \times \frac{\Delta p}{\ln(1+h)}, \tag{6.1h}$$

where $\Delta p := p_{\mathrm{IO}} - p_{\mathrm{ev}}$ and, for any $z \in \mathbb{R}$, $\mathrm{Be}(z) := z/(e^z - 1)$ is the inverse of the Bernoulli function of z such that $\mathrm{Be}(0) = 1$. The VFR of AH across the TM thickness is as follows:

$$Q(r) = V(r)2\pi r L_{\mathrm{TM}} = 2\pi L_{\mathrm{TM}}\frac{\kappa_0}{\mu_{fl}}\left(\mathrm{Be}\left[-M\frac{\Delta p}{\Delta p_b}\right]\right)^{-1}\frac{\Delta p}{\ln(1+h)}, \qquad r \in \Omega_r, \tag{6.1i}$$

where $h := t_{\mathrm{TM}}/r_{\mathrm{AC}}$. Relation (6.1i) shows that the VFR is constant, consistent with mass conservation. Some little algebra leads to the following nonlinear Ohm's law relating the AH pressure drop across the TM to the AH VFR across the TM

$$\Delta p = \frac{\mu_{fl} t_{\mathrm{TM}}}{\kappa_0 A_{\mathrm{TM}}} \times \frac{\ln(1+h)}{h} \times \mathrm{Be}\left[-M\frac{\Delta p}{\Delta p_b}\right] \times Q_{\mathrm{TM}}, \tag{6.1j}$$

where Q_{TM} is the value of the constant AH VFR across the TM and $A_{\mathrm{TM}} = 2\pi r_{\mathrm{AC}} L_{\mathrm{TM}}$ is the area of the TM in contact with the aqueous region.

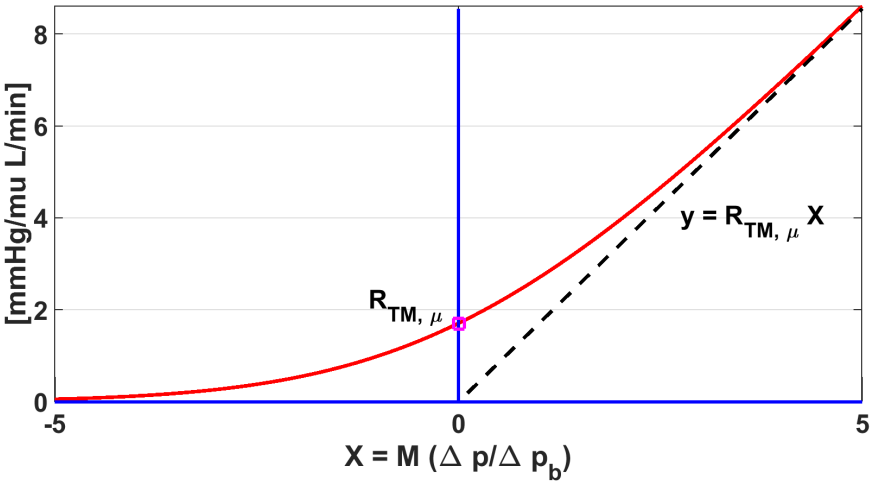

Figure 6. Plot of $R_{\mathrm{TM}}(\Delta p)$.

Comparing (6.1j) to (2.1e), we conclude that the TM hydraulic resistance has the following expression:

$$R_{\mathrm{TM}}(\Delta p) = R_{\mathrm{TM},\mu} \times \mathrm{Be}\left[-M\frac{\Delta p}{\Delta p_b}\right], \tag{6.1k}$$

where

$$R_{\mathrm{TM},\mu} = \frac{\mu_{fl} t_{\mathrm{TM}}}{\kappa_0 A_{\mathrm{TM}}} \times \frac{\ln(1+h)}{h} \tag{6.1l}$$

is the TM resistance to AH outflow at the microscale level. Figure 6 shows that R_{TM} is monotonically increasing with the pressure drop Δp across the TM thickness. We also notice that, for sufficiently large (and positive) values of Δp, the TM outflow resistance grows linearly with the difference between IOP and the episcleral venous pressure. This result is consistent with the model for R_{TM} developed in [36] by best fit with experimental data.

6.2. Including trabecular meshwork stiffness in the model for R_{TM}

Experimental findings from [19, 21] and [20] show that human trabecular meshwork stiffness in normal eyes may differ from that in glaucomatous eyes and that this difference may play a role in the pathogenesis of ocular hypertension in glaucoma. Denoting by C the function representing the outflow facility of the TM (units: μL mmHg^{-1} min^{-1}), the following model of C as a function of E_{TM} is derived in [19]:

$$C(E_{\mathrm{TM}}) = A - B\,E_{\mathrm{TM}}, \qquad E_{\mathrm{TM}} \in I_E, \tag{6.2a}$$

where $A = 0.6042$, $B = 0.0053$, and $I_E = [50,\ 100]$ kPa. Relation (6.2a) is the best fit of postmortem measurements of the TM outflow facility on perfused enucleated eyes from five normal and three

glaucomatous individuals aged between 74 and 88 years, after a post-processing of the measured data through an inverse finite element modeling approach.

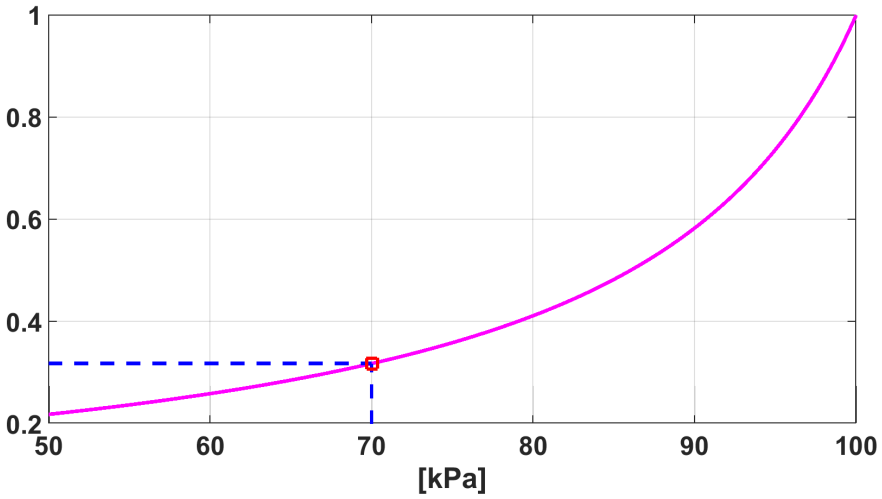

Figure 7. Plot of the dimensionless shape function $\eta_{\mathrm{TM}}(E_{\mathrm{TM}})$, for $E_{\mathrm{TM}} \in [50,\ 100]$ kPa. The red square indicates the value of η_{TM} in correspondance of the TM stiffness of a normal eye (equal to 70 kPa).

We apply (2.1d) to (6.2a) obtaining the following function:

$$\mathcal{R}(E_{\mathrm{TM}}) := (C(E_{\mathrm{TM}}))^{-1} = \frac{1}{A - B\,E_{\mathrm{TM}}}, \qquad E_{\mathrm{TM}} \in I_E. \tag{6.2b}$$

We see that $\mathcal{R}$ becomes singular for $E_{\mathrm{TM}} = A/B = 114$ kPa, so that (6.2b) is well defined for any $E_{\mathrm{TM}} \in I_E$. Letting $\mathcal{R}_{\max} := \max_{E \in I_E} |\mathcal{R}(E)|$, we define the dimensionless shape function as follows:

$$\eta_{\mathrm{TM}}(E_{\mathrm{TM}}) := \frac{\mathcal{R}(E_{\mathrm{TM}})}{\mathcal{R}_{\max}}, \qquad E_{\mathrm{TM}} \in I_E. \tag{6.2c}$$

Figure 7 shows a plot of η_{TM} in the interval I_E. It is worth noticing that η_{TM} is nonlinearly increasing with E_{TM} from the value 0.21875 to 1, with a percentage variation of more than 400%.

Under the assumption that the AH pressure drop across the TM and the stiffness of the TM tissue are independent and separable mechanisms, we can combine (6.1k) and (6.2c) to obtain the following macroscale model of the trabecular meshwork resistance:

$$R_{\mathrm{TM}}(\Delta p, E_{\mathrm{TM}}) = R_{\mathrm{TM},\mu} \times \mathrm{Be}\left[-M\frac{\Delta p}{\Delta p_b}\right] \times \eta_{\mathrm{TM}}(E_{\mathrm{TM}}), \tag{6.3}$$

where the microscale TM resistance $R_{\mathrm{TM},\mu}$ is defined in (6.1l).

7. Solution map

In Section 7.1, we write the nonlinear system (1.1) in matrix form, whereas in Section 7.2, we illustrate the algorithm for the solution of the nonlinear system via a fixed-point iteration.

7.1. The matrix form of the nonlinear system

Replacing into (1.1b) and (1.1c), the expressions of the AH VFRs derived in Sections 2–6, for a given value of E_{TM}, we obtain the following nonlinear algebraic system in matrix form:

$$\mathbf{M}(\mathbf{X})\mathbf{X} = \mathbf{b}(\mathbf{X}), \tag{7.1a}$$

where

$$\mathbf{M}(\mathbf{X}) = \begin{bmatrix} C_{\mathrm{CE}} + C_{\mathrm{CC}}(1 - \mathcal{K}_{act}) - C_{\mathrm{CE}} \\ -C_{\mathrm{CE}} + \mathcal{K}_{act}C_{\mathrm{CC}}C_{\mathrm{CE}} + C_{\mathrm{TM}}(\mathbf{X}; E_{\mathrm{TM}}) + C_{\mathrm{UV}} \end{bmatrix}, \tag{7.1b}$$

$$\mathbf{b}(\mathbf{X}) = \begin{bmatrix} C_{\mathrm{CE}}\Delta\Pi_{\mathrm{CE}} + C_{\mathrm{CC}}(1 - \mathcal{K}_{act})(\overline{p}_{\mathrm{CC}} - \Delta\Pi_{\mathrm{CC}}) \\ -C_{\mathrm{CE}}\Delta\Pi_{\mathrm{CE}} + \mathcal{K}_{act}C_{\mathrm{CC}}(\overline{p}_{\mathrm{CC}} - \Delta\Pi_{\mathrm{CC}}) + C_{\mathrm{TM}}(\mathbf{X}; E_{\mathrm{TM}})\overline{p}_{\mathrm{ev}} + C_{\mathrm{UV}}\overline{p}_{\mathrm{scs}} \end{bmatrix}. \tag{7.1c}$$

7.2. Fixed-point iteration

For any vector $\mathbf{Y} \in \mathbb{R}^2$, we define the residual associated with the nonlinear system (7.1a) as follows:

$$\mathbf{r}(\mathbf{Y}) = \mathbf{b}(\mathbf{Y}) - \mathbf{M}(\mathbf{Y})\mathbf{Y}. \tag{7.2a}$$

To numerically solve the nonlinear algebraic system (7.1a), for a given value of E_{TM}, we adopt the following fixed-point (FP) iteration of Richardson type (see [37, Chapter 4]):
given $\mathbf{X}^{(0)} \in \mathbb{R}^2$, for every $k \geq 0$ until convergence, compute

$$\mathbf{X}^{(k+1)} = \mathbf{T}_{\mathbf{M}}(\mathbf{X}^{(k)}), \tag{7.2b}$$

where, for $\alpha \neq 0$, the FP map is defined as

$$\mathbf{T}_{\mathbf{M}}(\mathbf{Y}) = \mathbf{B}_{\alpha}(\mathbf{Y})\mathbf{Y} + \mathbf{g}_{\alpha}(\mathbf{Y}), \tag{7.2c}$$

having introduced the iteration matrix

$$\mathbf{B}_{\alpha}(\mathbf{Y}) = \mathbf{I}_2 - \alpha\mathbf{P}^{-1}(\mathbf{Y})\mathbf{M}(\mathbf{Y}), \tag{7.2d}$$

and the affine term

$$\mathbf{g}_{\alpha}(\mathbf{Y}) = \alpha\mathbf{P}^{-1}(\mathbf{Y})\mathbf{b}(\mathbf{Y}). \tag{7.2e}$$

The symbol $\mathbf{I}_2$ denotes the identity matrix of order 2 whereas α and $\mathbf{P}$ are the acceleration parameter and the preconditioning matrix (shortly, "preconditioner"), respectively. The choice of the acceleration parameter and of the preconditioner determine the convergence properties of the FP iteration (7.2b). In what follows, we take $\alpha = 1$, while the following three different choices of the preconditioner are considered in the simulations described in Section 8:

$$\mathbf{P}(\mathbf{Y}) = \begin{cases} \texttt{diag}([C_{\mathrm{CE}} + C_{\mathrm{CC}}(1 - \mathcal{K}_{act}); C_{\mathrm{CE}} + C_{\mathrm{TM,b}} + C_{\mathrm{UV}}]) & \text{choice P1,} \\ \texttt{diag}([C_{\mathrm{CE}} + C_{\mathrm{CC}}(1 - \mathcal{K}_{act}); C_{\mathrm{CE}} + C_{\mathrm{TM}}(\mathbf{Y}; E_{\mathrm{TM}}) + C_{\mathrm{UV}}]) & \text{choice P2,} \\ \mathbf{M}(\mathbf{Y}) & \text{choice P3.} \end{cases} \tag{7.2f}$$

The `Matlab`-like notation `diag([A; B])` in (7.2f) is used to define a diagonal matrix of order 2 whose entries are `A` and `B`, respectively.

8. Results

In this section, we illustrate the results of the simulations conducted with the values of the parameters as in Appendices A and B. The TM stiffness E_{TM} is varied in the interval $\mathcal{I}_{\mathrm{TM}} = E_{\mathrm{ne}} \pm 50\% = [35,\ 105]$ kPa, where $E_{\mathrm{ne}} = 70$ kPa is TM Young's modulus reported in [19] for healthy eyes.

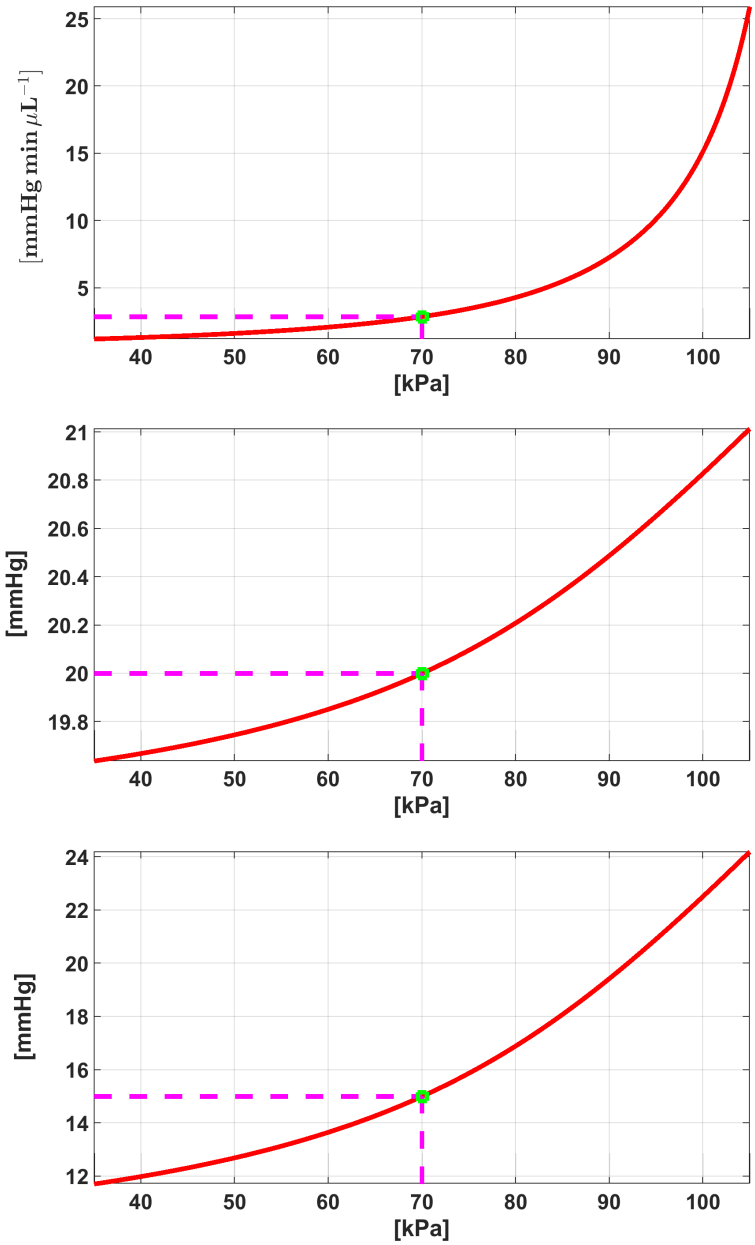

Figure 8. Top: plot of R_{TM} vs. E_{TM}. Middle: plot of p_{st} vs. E_{TM}. Bottom: plot of p_{IO} vs. E_{TM}. In each panel, $E_{\mathrm{TM}} \in [35,\ 105]$ kPa and the green-colored square indicates the value of the plotted variable in correspondance of the TM stiffness of a normal eye (equal to 70 kPa).

Figure 8 shows the predicted distributions of the TM outflow resistance R_{TM} (top panel) and of the AH fluid pressures p_{st} and p_{IO} in the stroma (middle panel) and in the aqueous side (bottom

panel), respectively. The plot in the top panel of the figure indicates that the TM outflow resistance is exponentially increasing for a TM tissue stiffer than normal while slowly decreasing for a TM tissue softer than normal. This behavior reflects on the predicted AH fluid pressure in the stroma (middle panel) and in the aqueous side (bottom panel), which linearly increase for a TM tissue stiffer than normal while decreasing at a slower rate for a TM tissue softer than normal. We see that the predicted IOP reaches the upper limit of the normal range (21 mmHg) in correspondance of $E_{\mathrm{TM}} \simeq 95\,\mathrm{kPa}$, consistent with the experimental value of 98 kPa reported in [19] for glaucomatous eyes.

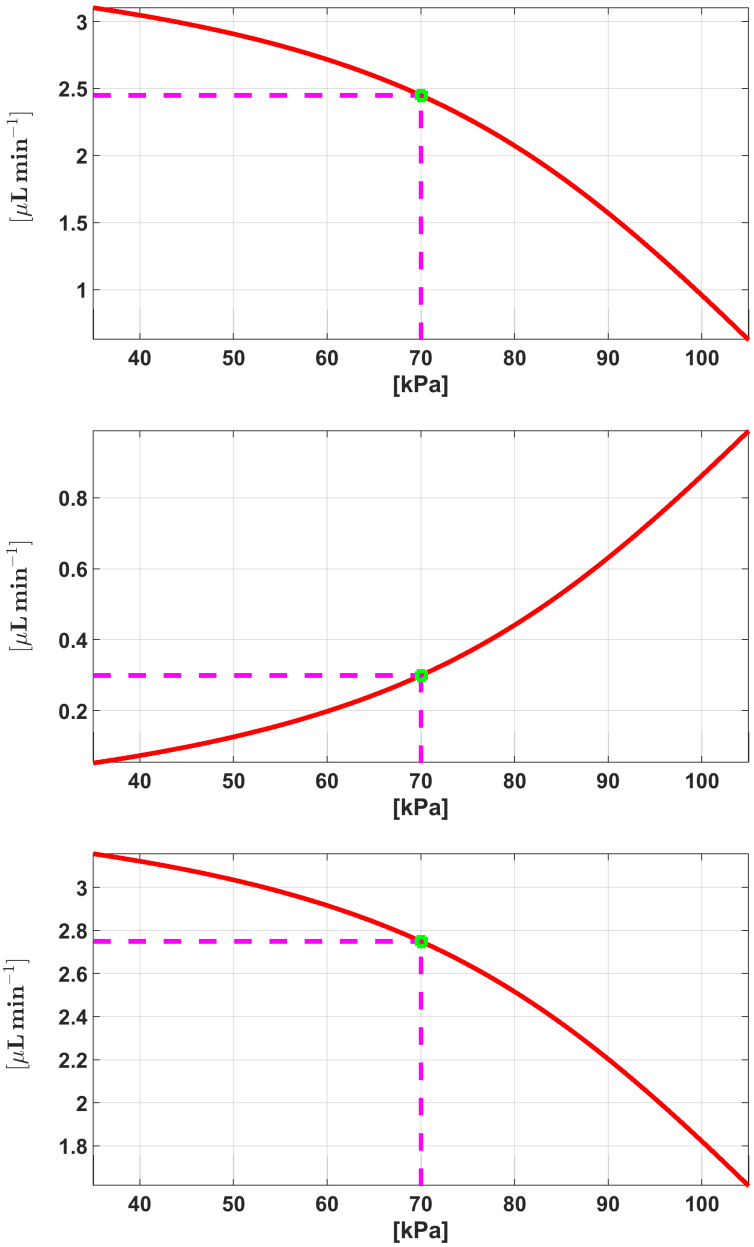

Figure 9. Top: plot of Q_{TM} vs. E_{TM}. Middle: plot of Q_{UV} vs. E_{TM}. Bottom: plot of Q_{AH} vs. E_{TM}. In each panel, $E_{\mathrm{TM}} \in [35,\ 105]\,\mathrm{kPa}$ and the green-colored square indicates the value of the plotted variable in correspondance of the TM stiffness of a normal eye (equal to 70 kPa).

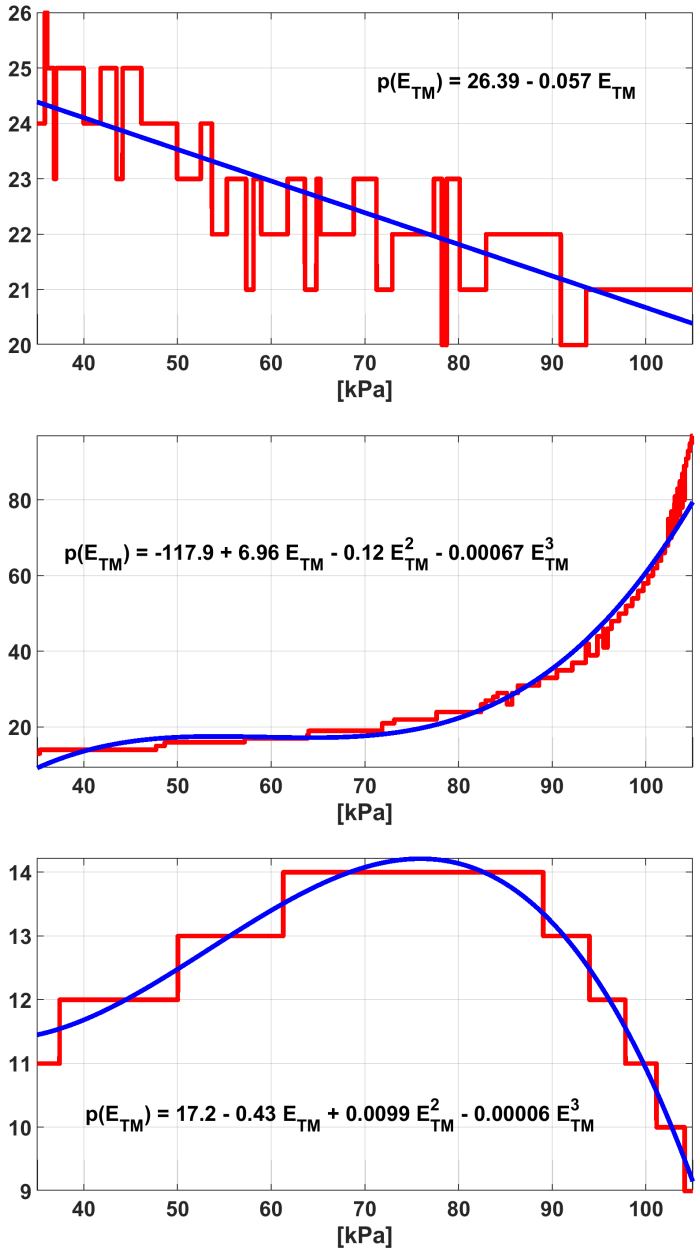

Figure 10. Plot of the number of iterations n_{iter} vs. E_{TM}. Choice for **P**: top: "P1"; middle: "P2"; bottom: "P3". The blue solid line represents the polynomial least-squares fit of n_{iter}. Linear fit is used for choice "P1", while cubic fit is used for choices "P2" and "P3".

Figure 9 shows the predicted distributions of the AH volumetric flow rates Q_{TM} (top panel) and Q_{UV} (middle panel) throughout the trabecular and uveoscleral outflow pathways, respectively, and of the AH volumetric flow rate Q_{AH} produced by the ciliary processes (bottom panel). The plot in the top panel of the figure indicates that the AH VFR across the trabecular outflow pathway nonlinearly decreases for a TM tissue stiffer than normal, consistent with the increased obstruction to AH flow due to R_{TM} increase, while being slowly increasing for a TM tissue softer than normal, consistent with R_{TM} decrease. A completely reverse behavior can be seen in the plot in the middle panel of the

figure which indicates that for a TM tissue softer than normal, Q_{UV} decreases because of the decreased TM outflow resistance which favors AH outflow through the TM pathway, whereas for a TM tissue stiffer than normal, Q_{UV} increases to compensate the amount of AH VFR which cannot be managed by the obstructed trabecular outflow pathway. This compensating behavior, adaptively depending on the stiffness of the TM tissue, mathematically represents the mechanism of the UV pathway to act as an adaptive "relief valve" for AH drainage described and analyzed in [15]. The plot in the bottom panel of the figure indicates that the AH produced in the case of a glaucomatous eye (assumed equal to $E_{\mathrm{TM}} = 98\,\mathrm{kPa}$) undergoes a decrease of 30 % with respect to the normal eye value of $2.75\,\mu\mathrm{L\,min^{-1}}$, consistent with the compensation mechanism elicited in the eye as a response to IOP increase (see [3]).

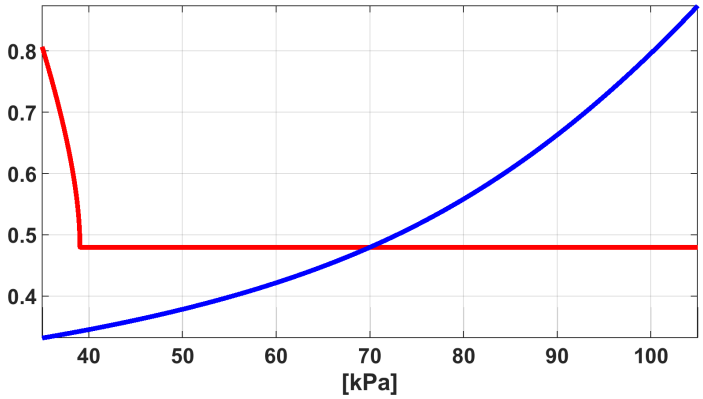

Figure 11. Plot of the spectral radius of the iteration matrix $\mathbf{B}_\alpha$ vs. E_{TM}. Choice for $\mathbf{P}$: red solid line: "P1"; blue solid line: "P2".

Figure 10 shows the number of iterations required by the FP iteration (7.2b) to reach convergence up to a relative increment between consecutive iterations equal to 10^{-6}. Results indicate that:

(a) the best performance of the algorithm is achieved using choice "P3" for the preconditioner (see the blue-colored solid line in the bottom panel of Figure 10);

(b) the second best performance is achieved using choice "P1" for the preconditioner (see the blue-colored solid line in the top panel of Figure 10);

(c) the worst performance is achieved using choice "P2" for the preconditioner (see the blue-colored solid line in the middle panel of Figure 10).

The explanation for (a) is that in the case "P3" we have $\mathbf{B}_\alpha(\mathbf{Y}) = \mathbf{0}_2$, where $\mathbf{0}_2$ is the zero matrix of order 2, so that the FP iteration (7.2b) becomes the following:

$$\mathbf{X}^{(k+1)} = \left[\mathbf{M}(\mathbf{X}^{(k)})\right]^{-1} \mathbf{b}(\mathbf{X}^{(k)}), \qquad k \geq 0, \tag{8.1}$$

which coincides with the solution of (7.1a), where $\mathbf{M}(\mathbf{X})$ and $\mathbf{b}(\mathbf{X})$ are approximated by $\mathbf{M}(\mathbf{X}^{(k)})$ and $\mathbf{b}(\mathbf{X}^{(k)})$, respectively. To analyze (b) and (c), let us consider the solution of a square linear system using a Richardson-type FP iteration with iteration matrix $\mathbf{B}$. The spectral radius ρ of $\mathbf{B}$ is defined as $\rho(\mathbf{B}) = \max_{\lambda \in \mathrm{sp}(\mathbf{B})} |\lambda|$ (see [37, Chapter 1]), where $\mathrm{sp}(\mathbf{B})$ is the spectrum of $\mathbf{B}$, i.e., the set of the eigenvalues λ of $\mathbf{B}$. The convergence rate η of the Richardson-type FP iteration is defined as $\eta = -\ln(\rho(\mathbf{B}))$

(see [37, Chapter 4]). Figure 11 shows the plot of $\rho(\mathbf{B}_\alpha)$ in the case of choices "P1" (solid red line) and "P2" (solid blue line). We can see that ρ in the case "P2" is smaller than ρ in the case "P1" for $E_{\mathrm{TM}} \leq E_{\mathrm{ne}}$, which explains why the number of iterations required to converge in the case "P2" is smaller than in the case "P1" for $E_{\mathrm{TM}} \leq E_{\mathrm{ne}}$. Conversely, ρ in the case "P2" is larger than ρ in the case "P1" for $E_{\mathrm{TM}} > E_{\mathrm{ne}}$, which explains why the number of iterations required to converge in the case "P2" is larger than in the case "P1" for $E_{\mathrm{TM}} > E_{\mathrm{ne}}$.

9. Discussion

IOP control through the use of therapeutic medications and, in extreme cases, surgery interventions, is fundamental to prevent and/or stabilize the progression of severe ocular diseases such as glaucoma. The adoption of mathematical and computational modeling as a theoretical complement to in vivo and/or in vitro studies has received considerable attention over the last decades [7, 8, 15, 24, 38–41]. In this respect, we develop in this article a multiscale model of the anterior segment of the human eye based on the coupling between the macroscale level, represented by an equivalent electric circuit, and the microscale level, represented by the porous microstructure of the TM outflow pathway. The process of coupling across scales leverages the introduction of a TM hydraulic resistance R_{TM} depending nonlinearly on the AH pressure difference Δp between aqueous side and episcleral vein and the TM mechanical stiffness E_{TM}. The numerical solution of the system of nonlinear algebraic equations arising from the application of Kirchoff current law at the circuit nodes is conducted by means of a functional iteration whose fixed point is the equilibrium value of the IOP.

The use of an equivalent electric representation of the anterior segment of the eye is not a novelty of this article (see [22, 24, 39, 40]), nor is the assumption of modeling the TM tissue as a biphasic porous deformable mixture (see [16, 42, 43]). The advancement of knowledge contributed by this work is having combined in the theoretical model of the TM hydraulic permeability κ: (*i*) a definition of TM dilatation proportional to Δp; and (*ii*) the experimental data from individuals in healthy and glaucomatous conditions obtained in [19]. The hybrid approach of merging continuum fluid mechanics and measurements allowed us to adapt to ophthalmology the dilatation-based model of κ proposed in [17, 44], obtaining a novel mathematical representation of R_{TM} as a function of Δp and E_{TM}.

The importance of having developed a model of the AH facility in the conventional TM outflow pathway depending on fluid and mechanical parameters is twofold. On the one hand, the model is consistent with fundamental principles of physiology [5]. On the other hand, the model is capable of (A) accounting for ageing effects by means of the dependence of R_{TM} on the Young modulus of the solid constituent of the mixture; and (B) responding in an adaptive manner to changes in the pressure field within the aqueous side of the eye by means of the dependence of R_{TM} on the pressure difference between aqueous side and episcleral vein. This description of the TM tissue provides a fluid-mechanical interpretation to the regulatory feedback mechanism for IOP homeostasis proposed in [45] and based on the hypothesis that TM cells sense increases in IOP as stretching or distortion of their extracellular matrix (ECM) and respond by increasing ECM turnover enzymes.

Feature (A) of the model is reflected in the top panel of Figure 8 which shows a five-fold increase of TM hydraulic resistance with respect to control conditions as a result of an increase of TM Young's modulus up to values occurring with patients affected by glaucoma. This finding suggests that potential drainage degradation of the extracellular TM matrix due to remodeling mechanisms may be directly

related to ageing through TM stiffening (see [46]).

Feature (B) of the model is reflected in the middle panel of Figure 9, which shows an almost three-fold increase of the unconventional outflow pathway with respect to control conditions as a result of an increase of TM Young's modulus up to values occurring with patients affected by glaucoma. This finding supports the conjecture that the orchestrated action of conventional and unconventional outflow pathways acts as an adaptive route to aqueous drainage sensitive to a fluid-mechanical stress (see [13] and [15]).

10. Conclusions and perspectives

In this article, we developed a computational virtual laboratory (CVL) for the simulation of AH dynamics in the human eye. The use of a mathematical model and a computational procedure is motivated by the need of supporting a modern precision medicine with a theoretically sound formulation that may be easily applicable in the context of a routine clinical environment.

Model formulation is based on physical principles and includes the interplay among fluid, mechanical and electrochemical forces to determine the formation of intraocular pressure. The algorithm simplicity and computational cost significantly benefit from the adoption of model reduction based on the analogy between electric and fluid variables, that allowed us to translate a time-dependent, nonlinearly coupled system of PDEs (Velocity-Extended Poisson-Nernst-Planck equations to describe solute and water fluid motion, plus nonlinear poroelastic equations to describe the motion of the watery fluid throughout a deformable porous trabecular meshwork structure) into a system of two nonlinearly coupled algebraic equations to determine the AH pressure in the ciliary stroma and in the aqueous side.

Despite these computational advantages, the model has several limitations:

- differential anatomy should be taken into account, in relation with age, gender, and ethnicity (see [47]);
- the CVL should include the contribution of the cornea to net water exchange between tear film and anterior chamber as well as the absorption and diffusion of an externally administered topical drug;
- the impact of JCT remodeling and the value of the constant M in Eq (5.2) should be taken into account in a more advanced mathematical representation of TM hydraulic permeability;
- the assumption that the AH pressure drop across the TM and the stiffness of the TM tissue are independent and separable mechanisms, at the basis of the validity of Eq (6.3), should be investigated by a systematic verification of model predictions against a wider set of clinical data;
- the representation of the UV outflow pathway should be expanded to include more advanced elements of ocular physiology into the characterization of R_{UV} (see [28]);
- autoregulatory mechanisms in the ciliary body should be considered to represent the situation in which the eye may be capable of increasing the outflow facility in response to a demand of increasing aqueous flow (see [48]);
- nano and microscales should be included in the circuit block of the CE, to provide a more refined description of AH production;
- the dependence on the time variable is neglected and should be taken into account in a more advanced version of the model to describe non-stationary effects such as (a) peak-to-peak IOP oscillations associated with the ocular pulse and consequent dependence on axial length of dynamic contour tonometry measurements (see [49]), and (b) transient IOP elevations due to saccadic eye

movements and blinking, which induce Schlemm's canal to mechanically behave as a collapsible conduit (see [50]).

The next steps of our research will be devoted to overcoming the above mentioned limitations through a combined use of mechanism-driven modeling and artificial intelligence techniques, with the final goal of employing the proposed CVL as a supporting tool to data analysis and interpretation of animal models and in vivo experiments [51].

Use of AI tools declaration

The authors declare they have not used Artificial Intelligence (AI) tools in the creation of this article.

Acknowledgments

This work was partially supported by NIH grants R01EY030851 and R01EY034718, NSF grants 2108711/2327640 and 2412130, NYEE Foundation grants, The Glaucoma Foundation, and in part by a Challenge Grant award from Research to Prevent Blindness, NY. Professor Alon Harris is supported by NIH grants (R01EY030851 and (R01EY034718), NYEE Foundation grants, The Glaucoma Foundation, and in part by a Challenge Grant award from Research to Prevent Blindness, NY. Dr. Alice Verticchio is supported by NYEE Foundation grant. The funders had no role in the design of the study; in the collection, analyses, or interpretation of data; in the writing of the manuscript; or in the decision to publish the results.

Conflict of interest

The authors declare there is no conflict of interest.

References

1. A. Thomas, A. A. Aref, Q. N. Cui, *Disability in Glaucoma*, 2023. Available from: https://eyewiki.org/Disability_In_Glaucoma#Reading.
2. M. Vidal-Sanz, F. J. Valiente-Soriano, A. Ortín-Martínez, F. M. Nadal-Nicolás, M. Jiménez-López, M. Salinas-Navarro, et al., Retinal neurodegeneration in experimental glaucoma, *Prog. Brain Res.*, **220** (2015), 1–35. https://doi.org/10.1016/bs.pbr.2015.04.008
3. S. G. Asrani, E. J. McGlumphy, L. A. Al-Aswad, C. J. Chaya, S. Lin, D. C. Musch, et al., The relationship between intraocular pressure and glaucoma: An evolving concept, *Prog. Retinal Eye Res.*, **103** (2024), 101303. https://doi.org/10.1016/j.preteyeres.2024.101303
4. R. Ramakrishnan, S. R. Krishnadas, M. Khurana, A. L. Robin, Aqueous humor dynamics, in *Diagnosis & Management of Glaucoma*, Jaypee Brothers Medical Publishers (P) Ltd., Rijeka, 2006.
5. A. Bill, E. H. Barany, Gross facility, facility of conventional routes, and pseudofacility of aqueous humor outflow in the cynomolgus monkey: The reduction in aqueous humor formation rate caused by moderate increments in intraocular pressure, *Arch. Ophthalmol.*, **75** (1966), 665–673. https://doi.org/10.1001/archopht.1966.00970050667017

6. R. F. Brubaker, Flow of aqueous humor in humans, *Invest. Ophthalmol. Visual Sci.*, **32** (1991), 3145–3166.
7. J. W. Kiel, Physiology of the intraocular pressure, in *Pathophysiology of the Eye: Glaucoma* (ed. J. Feher), Budapest, **4** (1998), 109–144. https://doi.org/10.1016/S0010-4655(98)00007-1
8. N. A. Delamare, Ciliary body and ciliary epithelium, *Adv. Organ Biol.*, **1** (2005), 127–148. https://doi.org/10.1016/S1569-2590(05)10005-6
9. R. Sacco, G. Guidoboni, A. G. Mauri, *A Comprehensive Physically Based Approach to Modeling in Bioengineering and Life Sciences*, Elsevier, Academic Press, Cambridge MA 02139, USA, 2019.
10. R. F. Brubaker, Importance of outflow facility, *Int. Glaucoma Rev.*, **3** (2001), 5.
11. R. F. Brubaker, Targeting outflow facility in glaucoma management, *Surv. Ophthalmol.*, **48** (2003), S17–S20. https://doi.org/10.1016/S0039-6257(03)00003-1
12. R. F. Ramos, W. D. Stamer, Effects of cyclic intraocular pressure on conventional outflow facility, *Invest. Ophthalmol. Visual Sci.*, **49** (2008), 275–281. https://doi.org/10.1167/iovs.07-0863
13. P. B. Liton, P. Gonzalez, Stress response of the trabecular meshwork, *J. Glaucoma*, **17** (2008), 378–385. https://doi.org/10.1097/IJG.0b013e31815f52a8
14. J. M. Sherwood, W. D. Stamer, D. R. Overby, A model of the oscillatory mechanical forces in the conventional outflow pathway, *J. R. Soc. Interface*, **16** (2019), 20180652. https://doi.org/10.1098/rsif.2018.0652
15. C. Costagliola, R. dell'Omo, L. Agnifili, S. Bartollino, A. M. Fea, M. G. Uva, et al., How many aqueous humor outflow pathways are there, *Surv. Ophthalmol.*, **65** (2020), 144–170. https://doi.org/10.1016/j.survophthal.2019.10.002
16. R. Avtar, R. Srivastava, Modelling aqueous humor outflow through trabecular meshwork, *Appl. Math. Comput.*, **189** (2007), 734–745. https://doi.org/10.1016/j.amc.2006.11.109
17. W. M. Lai, V. C. Mow, Drag-induced compression of articular cartilage during a permeation experiment, *Biorheology*, **17** (1980), 111–123. https://doi.org/10.1179/caj.1980.17.2.111
18. M. H. Holmes, V. C. Mow, The nonlinear characteristics of soft gels and hydrated connective tissues in ultrafiltration, *J. Biomech.*, **23** (1990), 1145–1156. https://doi.org/10.1016/0021-9290(90)90007-P
19. K. Wang, M. A. Johnstone, C. Xin, S. Song, S. Padilla, J. A. Vranka, et al., Estimating human trabecular meshwork stiffness by numerical modeling and advanced OCT imaging, *Invest. Ophthalmol. Visual Sci.*, **58** (2017), 4809–4817. https://doi.org/10.1167/iovs.17-22175
20. J. A. Last, T. Pan, Y. Ding, C. M. Reilly, K. Keller, T. S. Acott, et al., Elastic modulus determination of normal and glaucomatous human trabecular meshwork, *Invest. Ophthalmol. Visual Sci.*, **52** (2011), 2147–2152. https://doi.org/10.1167/iovs.10-6342
21. K. Wang, A. T. Read, T. Sulchek, C. R. Ethier, Trabecular meshwork stiffness in glaucoma, *Exp. Eye Res.*, **158** (2017), 3–12. https://doi.org/10.1016/j.exer.2016.07.011
22. J. W. Kiel, M. Hollingsworth, R. Rao, M. Chen, H. A. Reitsamer, Ciliary blood flow and aqueous humor production, *Prog. Retinal Eye Res.*, **30** (2011), 1–17. https://doi.org/10.1016/j.preteyeres.2010.08.001

23. E. H. Starling, On the absorption of fluids from the connective tissue spaces, *J. Physiol.*, **19** (1896), 312–326. https://doi.org/10.1113/jphysiol.1896.sp000596
24. A. B. Friedland, A hydrodynamic model of aqueous flow in the posterior chamber of the eye, *Bull. Math. Biol.*, **40** (1978), 223–235. https://doi.org/10.1016/S0092-8240(78)80041-X
25. M. Johnson, D. R. Overby, W. D. Stamer, C. R. Ethier, Scientific concerns about recent fluid-structure interaction models of the aqueous humor outflow pathway, *Invest. Ophthalmol. Visual Sci.*, **66** (2025), 18. https://doi.org/10.51202/2747-7096-2025-04-18
26. X. Cheng, P. M. Pinsky, The balance of fluid and osmotic pressures across active biological membranes with application to the corneal endothelium, *PLoS One*, **10** (2015), e0145422. https://doi.org/10.1371/journal.pone.0145422
27. M. Goel, R. G. Picciani, R. K. Lee, S. K. Bhattacharya, Aqueous humor dynamics: A review, *Open Ophthalmol. J.*, **4** (2010), 52–59. https://doi.org/10.3917/spi.052.0059
28. A. Llobet, X. Gasull, A. Gual, Understanding trabecular meshwork physiology: A key to the control of intraocular pressure, *Physiology*, **18** (2003), 205–209. https://doi.org/10.1152/nips.01443.2003
29. M. Johnson, E. R. Tamm, Biomechanics of aqueous humor outflow resistance, *Encycl. Eye*, **2010** (2010), 173–182. https://doi.org/10.1016/B978-0-12-374203-2.00093-2
30. W. K. McEwen, Application of poiseuille's law to aqueous outflow, *AMA Arch. Ophthalmol.*, **60** (1958), 290–294. https://doi.org/10.1001/archopht.1958.00940080306017
31. C. A. Rasmussen, P. L. Kaufman, The trabecular meshwork in normal eyes and in exfoliation glaucoma, *J. Glaucoma*, **23** (2014), S15–S19. https://doi.org/10.1097/IJG.0000000000000106
32. C. R. Ethier, R. D. Kamm, B. A. Palaszewski, M. C. Johnson, T. M. Richardson, Calculations of flow resistance in the juxtacanalicular meshwork, *Invest. Ophthalmol. Visual Sci.*, **27** (1986), 1741–1750.
33. F. Boschetti, G. Pennati, F. Gervaso, G. M. Peretti, G. Dubini, Biomechanical properties of human articular cartilage under compressive loads, *Biorheology*, **41** (2004), 159–166. https://doi.org/10.1177/0006355X2004041003004001
34. L. Bociu, G. Guidoboni, R. Sacco, J. T. Webster, Analysis of nonlinear poro-elastic and poro-visco-elastic models, *Arch. Ration. Mech. Anal.*, **222** (2016), 1445–1519. https://doi.org/10.1007/s00205-016-1024-9
35. L. Bociu, G. Guidoboni, R. Sacco, M. Verri, On the role of compressibility in poroviscoelastic models, *Math. Biosci. Eng.*, **16** (2019), 6167–6208. https://doi.org/10.3934/mbe.2019308
36. R. F. Brubaker, The effect of intraocular pressure on conventional outflow resistance in the enucleated human eye, *Invest. Ophthalmol. Visual Sci.*, **14** (1975), 286–292.
37. A. Quarteroni, R. Sacco, F. Saleri, *Numerical Mathematics*, 2nd Edition, Texts in Applied Mathematics, Springer, Berlin, Heidelberg, 2007.
38. R. Sacco, G. Guidoboni, J. W. Jerome, G. Bonifazi, N. M. Marazzi, A. C. Verticchio Vercellin, et al., A theoretical approach for the electrochemical characterization of ciliary epithelium, *Life*, **10** (2020), 8. https://doi.org/10.3390/life10020008

39. M. Dvoriashyna, A. J. E. Foss, E. A. Gaffney, R. Repetto, A mathematical model of aqueous humor production and composition, *Invest. Ophthalmol. Visual Sci.*, **63** (2022), 1. https://doi.org/10.1167/iovs.63.9.1
40. R. Sacco, G. Chiaravalli, G. Antman, G. Guidoboni, A. Verticchio, B. Siesky, et al., The role of conventional and unconventional adaptive routes in lowering of intraocular pressure: Theoretical model and simulation, *Phys. Fluids*, **35** (2023), 061902. https://doi.org/10.1063/5.0151091
41. J. A. Ferreira, P. de Oliveira, P. M. da Silva, J. N. Murta, Numerical simulation of aqueous humor flow: From healthy to pathologic situations, *Appl. Math. Comput.*, **226** (2014), 777–792. https://doi.org/10.1016/j.amc.2013.10.070
42. M. Johnson, J. M. Tarbell, A biphasic, anisotropic model of the aortic wall, *J. Biomech. Eng.*, **123** (2000), 52–57. https://doi.org/10.1115/1.1339817
43. W. J. McCarty, M. Johnson, The hydraulic conductivity of matrigel, *Biorheology*, **44** (2007), 303–317. https://doi.org/10.1177/0006355X2007044005006003
44. W. M. Lai, V. C. Mow, V. Roth, Effects of nonlinear strain-dependent permeability and rate of compression on the stress behavior of articular cartilage, *J. Biomech. Eng.*, **103** (1981), 61–66. https://doi.org/10.1115/1.3138261
45. J. M. B. Bradley, M. J. Kelley, X. Zhu, A. M. Anderssohn, J. P. Alexander, T. S. Acott, Effects of mechanical stretching on trabecular matrix metalloproteinases, *Invest. Ophthalmol. Visual Sci.*, **42** (2001), 1505–1513.
46. B. Liu, S. McNally, J. I. Kilpatrick, S. P. Jarvis, C. J. O'Brien, Aging and ocular tissue stiffness in glaucoma, *Surv. Ophthalmol.*, **63** (2018), 56–74. https://doi.org/10.1016/j.survophthal.2017.06.007
47. A. Belamkar, A. Harris, F. Oddone, A. V. Vercellin, A. Fabczak-Kubicka, B. Siesky, Asian race and primary open-angle glaucoma: Where do we stand, *J. Clin. Med.*, **11** (2022), 2486. https://doi.org/10.3390/jcm11092486
48. V. Gulati, D. A. Ghate, C. B. Camras, C. B. Toris, Correlations between parameters of aqueous humor dynamics and the influence of central corneal thickness, *Invest. Ophthalmol. Visual Sci.*, **52** (2011), 920–926. https://doi.org/10.1167/iovs.10-5494
49. C. Kaufmann, L. M. Bachmann, Y. C. Robert, M. A. Thiel, Ocular pulse amplitude in healthy subjects as measured by dynamic contour tonometry, *Arch. Ophthalmol.*, **124** (2006), 1104–1108. https://doi.org/10.1001/archopht.124.8.1104
50. J. C. Downs, C. F. Burgoyne, W. P. Seigfreid, J. F. Reynaud, N. G. Strouthidis, V. Sallee, 24-hour IOP telemetry in the nonhuman primate: Implant system performance and initial characterization of IOP at multiple timescales, *Invest. Ophthalmol. Visual Sci.*, **52** (2011), 7365–7375. https://doi.org/10.1167/iovs.11-7955
51. G. Guidoboni, R. Nunez, J. Keller, C. Wikle, E. L. Robinson, A. Verticchio, et al., Precision medicine and glaucoma management: How mathematical modeling and artificial intelligence help in clinical practice, *Expert Rev. Ophthalmol.*, **17** (2022), 299–301. https://doi.org/10.1080/17469899.2022.2130249

52. M. Shahidullah, W. H. Al-Malki, N. A. Delamere, Mechanism of aqueous humor secretion, its regulation and relevance to glaucoma, in *Glaucoma-Basic and Clinical Concepts*, IntechOpen, 2011.

53. A. T. Layton, A. Edwards, *Mathematical Modeling in Renal Physiology*, Lecture Notes on Mathematical Modelling in the Life Sciences, Springer, Berlin, Heidelberg, 2014.

54. T. Krupin, P. S. Reinach, O. A. Candia, S. M. Podos, Transepithelial electrical measurements on the isolated rabbit iris-ciliary body, *Exp. Eye Res.*, **38** (1984), 115–123. https://doi.org/10.1016/0014-4835(84)90096-4

55. S. R. Pesin, *Na and Cl Fluxes, and Effects of Pharmacological Agents on the Short-circuit Current of the Isolated Rabbit Iris-ciliary Body*, Ph.D thesis, Yale University School of Medicine, 1985.

56. K. Emi, J. E. Pederson, C. B. Toris, Hydrostatic pressure of the suprachoroidal space, *Invest. Ophthalmol. Visual Sci.*, **30** (1989), 233–238. https://doi.org/10.1136/gut.30.2.233

57. M. Johnson, A. Shapiro, C. R. Ethier, R. D. Kamm, Modulation of outflow resistance by the pores of the inner wall endothelium, *Invest. Ophthalmol. Visual Sci.*, **33** (1992), 1670–1675.

Appendix

A. Data of solute components

The following substances are involved in the model of AH dynamics proposed in this article:

- 5 ion types: sodium, potassium, calcium (cations); chlorine and bicarbonate (anions);
- four solute types with low molecular weight: ascorbate, lactate, glucose, and urea;
- one solute type with high molecular weight: albumin.

Table 2. Solute molar densities in the aqueous side and in blood plasma. The value of pH in the plasma and in the aqueous side is 7.4 and 7.11, respectively (data taken from [52]).

Solute	Plasma	Units	Aqueous	Units
Na^+	137.5	mM	142	mM
K^+	4.25	mM	4	mM
Ca^{2+}	2.3	mM	1.2	mM
Cl^-	108.5	mM	131	mM
HCO_3^-	27	mM	20	mM
Ascorbate	0.05	mM	1.1	mM
Lactate	0.65	mM	4.5	mM
Glucose	6	mM	3.3	mM
Urea	4.9	mM	4.1	mM
Albumin	1.05	mM	0.0034	mM

Table 2 provides the values of the solute molar densities in the blood plasma and in the aqueous side, respectively. The values of the electro-neutralizing charged protein molar density are determined by enforcing the electroneutrality condition which yields $c_{X,\mathrm{pl}} = 10.85\,\mathrm{mM}$ in the blood plasma, with

$z_{X,\mathrm{pl}} = -1$, and $c_{X,\mathrm{aq}} = 2.6\,\mathrm{mM}$ with $z_{X,\mathrm{aq}} = +1$. The reflection coefficients across each membrane are defined as follows: $\sigma_\alpha = 2 \cdot 10^{-4}$ for each considered ion α; $\sigma_\beta = 10 \cdot 10^{-4}$ for each considered low molecular weight neutral solute β; $\sigma_\gamma = 0.5$ for the high molecular weight neutral solute γ; $\sigma_X = 1$ for the neutralizing charged protein. The above values of the reflection coefficients are not chosen on the basis of experimental studies because of the difficulty in accessing the subcellular scale, which would be necessary to measure the hydraulic permeability of the membranes constituting the boundary of the ciliary epithelial cellular double layer. For this reason, we follow the approach of [53, Chapter 8] and observe that every reflection coefficient σ is bounded between 0 and 1, with $\sigma = 0$ meaning that no reflection impedes solute passage across the membrane and $\sigma = 1$ meaning that solute passage is fully impeded. Naturally, these two limit behaviors depend on the molecular weight of the substance crossing the membrane, which explains why the values of σ_α are very close to zero, σ_β are small but larger than σ_α, whereas the value of σ_γ is much larger and closer to 1, and the value of σ_X is exactly equal to 1 because of the larger molecular weight of the fixed charged membrane proteins that ensure the electroneutrality of the intracellular bathing solution. Finally, the transepithelial potential difference (PD) is set equal to 2.5 mV (aqueous side negative, see [54, 55]). Inserting the values of the solute molar densities and reflection coefficients and of the PD into relation (3.7a) yields: $\Delta\Pi^{\mathrm{ec}}_{tot} = 2.545\,\mathrm{mmHg}$ at the CC-to-stroma interface; $\Delta\Pi^{\mathrm{ec}}_{tot} = -14.8032\,\mathrm{mmHg}$ at the stroma-to-aqueous interface; $\Delta\Pi^{\mathrm{ec}}_{tot} = 0\,\mathrm{mmHg}$ at the aqueous-to-TM and aqueous-to-UV interfaces.

B. Calibration of model parameters

Before describing the simulation results, we need to calibrate the values of model parameters, specifically determining:

(A) the values of the hydraulic resistances in the electric circuit of Figure 2;
(B) the value of the constant M.

B.1. Hydraulic resistances

Following [22], we set $p_{\mathrm{CC},b} = 25\,\mathrm{mmHg}$ (ciliary capillary), $p_{\mathrm{IO},b} = 15\,\mathrm{mmHg}$, and $p_{\mathrm{ev},b} = 11\,\mathrm{mmHg}$. Following [56], we set the suprachoroidal space pressure $p_{\mathrm{scs},b} = 8\,\mathrm{mmHg}$. Finally, we set $p_{\mathrm{st},b} = 20\,\mathrm{mmHg}$ (stroma). We also set the baseline value of the AH volumetric flow rate (VFR) and of the VFR across the TM and UV outflow pathways equal to $Q_b = 2.75\,\mu\mathrm{L\,min^{-1}}$, $Q_{\mathrm{TM},b} = 2.45\,\mu\mathrm{L\,min^{-1}}$, and $Q_{\mathrm{UV},b} = 0.3\,\mu\mathrm{L\,min^{-1}}$, respectively [22], and we set $\mathcal{K}_{act,b} = 0.85$ (based on the considerations made in [27]). Then, we use the continuity of current (equivalently, the volumetric flow rate) and Ohm's law to determine the value of the hydraulic resistances in the electric circuit of Figure 2:

$$R_{\mathrm{w}} = \frac{p_{\mathrm{CC},b} - p_{\mathrm{st},b}}{Q_b} = 0.8927\,\mathrm{mmHg\,min\,(\mu L)^{-1}}, \tag{B.1a}$$

$$R_{\mathrm{hyd}} = \frac{(p_{\mathrm{st},b} - p_{\mathrm{IO},b}) - \Delta\Pi^{\mathrm{ec}}_{tot}}{Q_b\,(1 - \mathcal{K}_{act,b})} = 47.9487\,\mathrm{mmHg\,min\,(\mu L)^{-1}}, \tag{B.1b}$$

$$R_{\mathrm{TM},b} = \frac{p_{\mathrm{IO},b} - p_{\mathrm{ev},b}}{Q_{\mathrm{TM},b}} = 2.8571\,\mathrm{mmHg\,min\,(\mu L)^{-1}}, \tag{B.1c}$$

$$R_{\mathrm{UV},b} = \frac{p_{\mathrm{IO},b} - p_{\mathrm{scs},b}}{Q_{\mathrm{UV},b}} = 13.3333\,\mathrm{mmHg\,min\,(\mu L)^{-1}}. \tag{B.1d}$$

B.2. The constant M

To determine M, we enforce the condition

$$R_{\mathrm{TM}}(\Delta P_{\mathrm{TM},b},\, E_{\mathrm{TM},b}) = R_{\mathrm{TM},b} \tag{B.2a}$$

where R_{TM} is computed using (6.3), while $\Delta P_{\mathrm{TM},b} = p_{\mathrm{IO},b} - p_{\mathrm{ev},b} = 7\,\mathrm{mmHg}$, $R_{\mathrm{TM},b}$ is given by (B.1c) and $E_{\mathrm{TM},b} = 70\,\mathrm{kPa}$ is the value of the TM stiffness for a normal eye (see [19]). The resulting nonlinear equation for M reads

$$\frac{-M}{\exp(-M) - 1} = \beta_M, \tag{B.2b}$$

having set

$$\beta_M := \frac{R_{\mathrm{TM},b}}{R_{\mathrm{TM},\mu}\eta_{\mathrm{TM}}(E_{\mathrm{TM},b})}, \tag{B.2c}$$

with $R_{\mathrm{TM},\mu}$ being defined in (6.11). The TM radial thickness is defined as $t_{\mathrm{TM}} = 10^{-5}\,\mathrm{m}$ (see [16]). The geometrical parameters of the TM tissue are defined as follows (see [25]): $r_{\mathrm{AC}} = 5.8 \cdot 10^{-3}\,\mathrm{m}$ and $L_{\mathrm{TM}} = 3 \cdot 10^{-4}\,\mathrm{m}$. The pore diameter is $d_p = 1.2 \cdot 10^{-6}\,\mathrm{m}$ and the surface pore density is $N_p = 835 \cdot 10^6\,\mathrm{pores\,m^{-2}}$, from which, using (5.3), we get $\Phi = 9.44 \cdot 10^{-4}$, which is in very good agreement with the typical value of TM porosity $\Phi = 10^{-3}$ considered in [57]. Setting $\mu_{fl} = 5.1852 \cdot 10^{-6}\,\mathrm{mmHg\,s}$, we get $\beta_M = 1.9304$, from which the solution of the nonlinear equation (B.2b) yields $M = 1.4994$.